

High-energy and long-life aluminum–sulfur battery: Employment of electrocatalytic function into continuous multiple reactions within quasi-solid-state electrolyte

Zheng Huang

University of Science and Technology Beijing

Wei Wang

University of Science and Technology Beijing

Wei-Li Song

Beijing Institute of Technology

Mingyong Wang

University of Science and Technology Beijing <https://orcid.org/0000-0002-5246-163X>

Hao-Sen Chen

Beijing Institute of Technology

Shuqiang Jiao (✉ sjiao@ustb.edu.cn)

University of Science and Technology Beijing

Daining Fang

Beijing Institute of Technology

Article

Keywords:

Posted Date: January 11th, 2022

DOI: <https://doi.org/10.21203/rs.3.rs-1203817/v1>

License:   This work is licensed under a Creative Commons Attribution 4.0 International License.

[Read Full License](#)

Abstract

Aluminum–sulfur (Al–S) batteries of ultrahigh energy-to-price ratios are promising for next-generation energy storage, while they suffer from large charge/discharge voltage hysteresis and short lifespan. Herein, an electrocatalyst-boosting quasi-solid-state Al–S battery is proposed, in which sulfur is anchored on the cobalt/nitrogen co-doped graphene (S@CoNG, as the positive electrode) and chloroaluminate-based ionic liquid (IL) is encapsulated into metal-organic frameworks (IL@MOF, as the quasi-solid-state electrolyte). Mechanistically, the Co–N bonds in CoNG act as electrocatalytic center to continuously induce breaking of Al–Cl bonds and S–S bonds and accelerate the kinetics of sulfur conversion, endowing the Al–S battery with much shortened voltage gap of 0.32 V and 0.98 V in the discharge voltage plateau. Within quasi-solid-state IL@MOF electrolytes, shuttle effect of polysulfides has been inhibited, which stabilizes the process of reversible sulfur conversion. Consequently, the assembled Al–S battery presents high specific capacity of 820 mAh g⁻¹ and 78% capacity retention after 300 cycles. This concept here offers novel insights to design practical Al–S batteries for stable energy storage.

1. Introduction

The ever-growing demand for economic and efficient utilization of renewable energy sources have impelled the exploration of advanced energy storage technologies.^{1,2} On account of the high theoretical capacity (2890 mAh g⁻¹) and abundant resource of aluminum, rechargeable aluminum batteries (RABs) have been considered as a promising candidate for next-generation energy storage systems.^{3,4} However, the traditional positive electrode materials of RABs are suffering from low specific capacity (i.e., carbon-based materials <120 mAh g⁻¹ and metallic compounds <300 mAh g⁻¹), and cannot well meet the requirement of high-energy density RABs.^{5,6} Sulfur is an emerging positive electrode material that possesses a gravimetric capacity of 1672 mAh g⁻¹, which has the potential to endow aluminum-sulfur (Al–S) battery with a high theoretical energy density of 1340 Wh kg⁻¹.^{7–9} Additionally, the low price and high abundance in nature of both aluminum and sulfur realize an incomparable energy-to-price ratios of Al–S battery, which provides an opportunity to break the bottleneck of RABs.^{10–13}

Unfortunately, although Al–S batteries are appealing, they are facing many challenging issues, including large charge/discharge voltage gap (>0.6 V), low Coulombic efficiency (<80%), and short lifespan (<20 cycles), resulting from intrinsic properties of sulfur and chloroaluminate-based ionic liquid (IL) electrolyte.^{8,10,14,15} Both sulfur reduction reaction (SRR, discharge process) and sulfur evolution reaction (SER, charge process) involve multi-electron transfer processes, which are sluggish kinetic response.^{16,17} Moreover, the energy barrier associated with the dissociation of Al³⁺ from Al ionic cluster (Al_xCl_y⁻) in IL electrolyte is also likely responsible for the slow kinetics, resulting in high charge/discharge voltage hysteresis.¹⁴ On the other hand, sulfur and its discharge product polysulfides are highly soluble in the electrolyte, and these dissolved sulfur-based substances have strong tendency to migrate out from the positive electrode region towards the negative electrode region during cycling. This irreversible migration is the so-called “shuttle effect”, leading to not only the active-material loss but also severe aluminum-

metal contamination, which is the origin of the low Coulombic efficiency and short cycle life of Al-S batteries.^{8,10,11} Referencing other sulfur-based battery systems, the utilization of (quasi-)solid-state electrolytes could effectively alleviate the shuttle effect of polysulfide and thus achieve stable cycling performance.¹⁸⁻²⁵ However, the sluggish kinetics in solid electrolytes becomes even worse than liquid ones, making it seem impossible to realize a practical (quasi-)solid-state Al-S battery. This is indeed the reality, and to the best of our knowledge, (quasi-)solid-state Al-S battery has not been reported so far. Similar to SRR and SER, the oxygen reduction reaction (ORR) in fuel cell and oxygen evolution reaction (OER) in electrochemically splitting water also undergo a high energy barrier, and usually require the introduction of different electrocatalysts, including metal, metal oxide, and doped carbon materials, to accelerate the reaction kinetics.²⁶⁻²⁹ Considering sulfur and oxygen in the same main group, some of these electrocatalysts could also be able to trigger and accelerate the multi-electron reaction of SRR and SER. Therefore, development of appropriate electrocatalysts may be a hopeful way to realize the practical (quasi-)solid-state Al-S batteries.

To achieve this goal, in this study we have proposed an efficient electrocatalyst for sulfur conversion reactions using cobalt-nitrogen co-doped graphene (CoNG), and a quasi-solid-state electrolyte via encapsulating IL into metal-organic frameworks (IL@MOF) for Al-S batteries. The doped Co-N structure is evenly distributed in CoNG nanosheet, which is further used as sulfur host (S@CoNG) for positive electrode. The Co-N construction serves as multifunctional catalytic centers to continuously induce the dissociation of Al^{3+} from Al_xCl_y^- ions and breaking of S-S bonds, and thus greatly accelerate the reaction kinetics of sulfur conversion. Consequently, the electrocatalyst-boosting S@CoNG positive electrode presents a low voltage hysteresis of 0.32 V and a high discharge plateau of 0.98 V, facilitating a high energy density. Furthermore, the rich and narrow channels of MOF in IL@MOF filled up with IL ions endow fast active ion transport and successfully inhibit the shuttle effect of polysulfides, which stabilizes the process of reversible sulfur conversion. Surprisingly, the quasi-solid-state Al-S batteries assembled with S@CoNG positive electrode and IL@MOF electrolyte deliver a high specific capacity of 820 mAh g⁻¹ in the first cycle and 78% capacity retention beyond 300 cycles. The electrocatalytic effect and quasi-solid-state electrolyte are the key to realize the high-energy and long-life Al-S batteries.

2. Results

2.1 The construction and electrochemical performance of quasi-solid-state Al-S batteries

The design principle of quasi-solid-state aluminum-sulfur (Al-S) batteries and its working mechanism are illustrated in Figure 1a. The cobalt-nitrogen co-doped graphene (CoNG) is elected as the sulfur host for positive electrode (S@CoNG), and the zirconium-based metal-organic frameworks (Uio-66, MOF) immersed in ionic liquid (IL@MOF) serve as the quasi-solid-state electrolyte for Al-S batteries. The CoNG can catalyze both the dissociation of the Al^{3+} and reactions of sulfur conversion. Meanwhile, the IL@MOF quasi-solid-state electrolyte plays a role in delivering active ions (AlCl_4^- and Al_2Cl_7^-) and inhibiting the

shuttle effect of polysulfide due to its narrow channels. The characterization and performance of CoNG electrocatalyst and IL@MOF quasi-solid-state electrolyte will be further discussed.

The quasi-solid-state Al-S batteries was assembled with composite positive electrode, in which the S@CoNG was mixed with IL@MOF and acetylene black (AB) and pressed into a circular pellet. The optimal composition of S@CoNG: IL@MOF: AB was first affirmed by galvanostatic charge and discharge processes (**Figure S1**). Apparently, the samples with S@CoNG: IL@MOF: AB ratios of 7: 6: 1 exhibit the highest discharge capacity ($\sim 820 \text{ mAh g}^{-1}$) and the smallest charge-discharge voltage gap ($\sim 0.43 \text{ V}$), and this positive electrode composition is used in the following tests. Figure 1b shows the cyclic voltammetry (CV) curves of the Al-S battery within the voltage range of 0.1–2.0 V. One cathodic peak at 0.81 V and two anodic peaks at 1.43 V and 1.59 V are observed in the first scan, which corresponds to the reduction of sulfur and the oxidation of sulfide, respectively.^{9,10} Simultaneously, the CV curves at subsequent scanning cycles show similar shape and size, representing a superior reversibility. Figure 1c demonstrates the initial three charge/discharge curves of the battery at a current density of 50 mA g^{-1} . One discharge voltage plateau appears at 0.83 V, and two charge voltage plateaus appear at 1.42 and 1.55 V in 1st cycle, in good agreement with the CV curves. Subsequently, a higher discharge voltage plateau at 0.90 V and only one charge voltage plateau at 1.33 V in subsequent two cycles are observed. The lower voltage hysteresis and reduced amount of charge voltage plateau may be attributed to improved electrolyte infiltration, and the sluggish ion transmission results in the two charge voltage plateaus in the first cycle. The electrochemical impedance spectroscopy (EIS) and corresponding distribution of relaxation times (DRT) analysis are employed to further investigate the reaction dynamics during the first few cycles. Before cycling, the Nyquist plots were composed of two depressed semicircles at high frequencies corresponding to the interfacial charge transfer resistance (R_{ct}). Whereas, after the initial cycle, only one semicircle remains and its radius decreases, meaning a reduced R_{ct} (**Figure S2a**). The DRT analysis confirms that the response time of ion diffusion has moved forward after cycling, thus resulting in sharp decrease of electrochemical reaction impedance (**Figure S2b**).³⁰ Therefore, the decreased R_{ct} may be due to the formation of a stable interface between the sulfur and IL@MOF electrolyte in composite positive electrode, which can also explain the change in voltage plateaus in the first two cycles.

Figure 1d shows the rate performance of the quasi-solid-state Al-S battery. It can deliver an overall capacity of 820 mA h g^{-1} at 50 mA g^{-1} , and the capacity of the sulfur positive electrode (not including doped graphene host) can reach as high as 1335 mA h g^{-1} calculated using the known sulfur weight ratio (61.4%, **Figure S3**). It is clear that the Al-S battery shows stable reversible capacities of 580, 450, and 202 mAh g^{-1} at the current densities of 100, 200, and 300 mA g^{-1} , respectively. Furthermore, the rate capability curves are highly reversible (no hysteresis) when cycled at the same rate (**Figure S4**), attributing to the efficient ion transport in the interface between the sulfur and solid-state electrolyte. In addition, the cycle performances of liquid-state and quasi-solid-state Al-S batteries are evaluated and compared (Figure 1e). For the liquid-state Al-S battery, although it can deliver a reversible capacity of 945 mAh g^{-1} in the first cycle (at a current density of 50 mA g^{-1}), the capacity remains at 175 mAh g^{-1} after only 100

cycles. The poor capacity retention of liquid-state battery is ascribed to the shuttle effect of polysulfides, as described in the previous reports.^{8,11,15} In comparison, the initial capacity of quasi-solid-state Al-S battery is slightly lower than that of liquid-state one, whereas it could still deliver a high capacity of 640 mAh g⁻¹ after 300 cycles with an excellent capacity retention of 78%, revealing a stable cycle stability. The superior cycle stability of quasi-solid-state Al-S batteries is attributed to the successful suppression of shuttle effect of polysulfide by IL@MOF quasi-solid-state electrolyte. Most importantly, compared to the documented RABs, the relation of specific capacity versus discharge potential of such quasi-solid-state Al-S battery implies that the performance is competitive with the record-setting values in terms of energy density (Figure 1f and Table S1).^{9,14,15,31-41}

2.2 The structure characterization and evolution of sulfur positive electrode

The morphology and structure of CoNG and S@CoNG are characterized by scanning electron microscopy (SEM) and transmission electron microscopy (TEM). The CoNG consists of a typical wrinkled sheet-like structure (Figure 2a), which is beneficial to sulfur loading. No obvious nanoparticles are found on the surface of the graphene sheet (Figure S5a), indicating the absence of residual Co particles in CoNG. Meanwhile, the elemental analysis reveals that Co, N and C elements are distributed in CoNG and these composition distributions are in accordance with the observed morphology (Figure S6). The SEM and TEM results indicate that the morphology of the CoNG composite remains intact after sulfur loading (Figure 2b), and the sulfur element is clearly detected in S@CoNG sample (Figure S5b and S7), thus confirming the successful loading of sulfur on S@CoNG. The S@CoNG powder was mixed with IL@MOF quasi-solid-state electrolyte and acetylene black and pressed to form the positive electrode (Figure 2c), and the three components in mixture are uniform dispersion and seamless contact to afford a favorable electron and ion transport network, guarantying a high-performance sulfur positive electrode.

X-ray photoelectron spectroscopy (XPS) is then used to analyze the valence state and chemical composition of C, N, and Co in CoNG. The C 1s XPS spectra can be fitted to three peaks centered at 284.8, 285.4, and 286.8 eV, corresponding to sp²-hybridized C-C, C-N, and C-O, respectively (Figure S8).⁴² Meanwhile, the N 1s spectra exhibit two major components (Figure 2d), which could be ascribed to pyridinic-N (398.5 eV) and graphitic-N (401.5 eV). Notably, a distinct peak located at 399.3 eV is indexed to the Co-N bond, suggesting that some of the nitrogen atoms are integrated into the graphene lattice along with cobalt atoms.^{43,44} Furthermore, in the Co 2p_{3/2} signal (Figure 2e), the peaks located at 780.5 eV and 782.5 eV are ascribed to Co-N₄ and Co-N, respectively, without any metallic Co signal (778.5 eV),^{45,46} indicating that cobalt enters the carbon skeleton mainly in the form of Co-N_x structures.

X-ray absorption near-edge structure (XANES) and extended X-ray absorption fine structure (EXAFS) spectroscopy were further conducted to analyze the coordination mode of Co atoms in CoNG. The results for standard samples including Co foil and Co₂O₃ were also probed as references. The XANES profile at the Co K-edge of CoNG is significantly different from those of the reference samples, and the pre-edge

peak at 7705–7715 eV of CoNG situates between Co foil and Co₂O₃ (marked by the dotted box in Figure 2f), indicating that Co atoms in CoNG are positively charged. As shown in Figure 2g, the Fourier-transformed EXAFS (FT-EXAFS) curve for CoNG exhibits one strong peak at about 1.45 Å, which is slightly shorter than Co–O (1.52 Å) distance in the standard Co₂O₃ sample, probably due to the dominated bonding between Co and N.⁴⁷ Meanwhile, a Co–Co peak (2.18 Å) is noticed for the standard Co foil, which is almost undetectable in CoNG, suggesting the absence of metallic Co in CoNG. Based on this observation, we performed the tetrahedral geometry (Co–N₄) structure model (inset in Figure 2h) to fit the FT-EXAFS curve of CoNG. The fitted coordination number of Co (3.8) in Figure 2h is in good agreement with tetrahedral Co–N₄ structure, and the calculated Co–N bond length is 1.82 Å (**Table S2**), indicating that Co atom coordinates with four N atoms with a scattering distance of 1.82 Å in CoNG.^{42,47} The k-spaces results confirm that the fitting result is in good agreement with the experimental data (**Figure S9**). To more clearly understand atomic dispersion of Co atom, the wavelet transform (WT) was performed to analyze the k²-weighted EXAFS signal in view of the powerful resolution in radial distance and k-space.⁴⁸ The Co foil shows one WT maximum intensity at 6.9 Å⁻¹ corresponding to Co–Co coordination, and Co₂O₃ has a WT maximum at 6.3 Å⁻¹ due to Co–Co and another WT maximum at 4.8 Å⁻¹ assigned to Co–O (**Figure S10**). For CoNG, the WT contour plot appears one intensity maximum at 4.7 Å⁻¹, corresponding to Co–N coordination (Figure 2i). Based on the above analysis, it can be concluded that Co atoms are atomically dispersed and coordinated with four N atoms to form Co–N₄ centers in CoNG.

Subsequently, the phase transition and structural evolution of S@CoNG positive electrode during charge and discharge processes were investigated. Before cycling, the X-ray diffraction (XRD) pattern of S@CoNG shows a series of characteristic diffraction peaks of sulfur and a weak carbon peak (**Figure S11**), representing a high sulfur loading. For the discharged sample, the peaks of sulfur disappear and are replaced by Al₂S₃, a discharging product in this system. When charging to 1.8 V, the characteristic peaks of sulfur reappear again, indicating a highly reversible electrochemical process. The evolution in the chemical state of sulfur during the charge and discharge processes is further investigated by *ex-situ* XPS and Raman spectrum (Figure 2j-l). During the discharge process, the signal of S shifts significantly toward a smaller binding energy, and the distinct peak of S^{x-} (163 eV, Al₂S_x) appears and gradually increases with discharge depth (Figure 2k), corresponding to the formation of polysulfides.^{49,50} During the subsequent charging process, the signal of S^{x-} gradually disappears until it returns to the original state, suggesting that the S^{x-} are continuously oxidized.⁵¹ Meanwhile, the reduction of sulfur undergoes several stages in the discharge process, in while the S₈ (468 cm⁻¹ and 512 cm⁻¹) molecules are first reduced to S₃⁻ (418 cm⁻¹) and then successively reduced to S₂⁻ (135 cm⁻¹), S⁻ (161 cm⁻¹), and the end product S²⁻ (190 cm⁻¹)^{52,53}, as shown in Figure 2l. Likewise, the reduction products S²⁻ are also progressively oxidized to form S⁻, S₂⁻, S₃⁻, and S₈ molecules in the charging process, revealing highly reversible redox process. The above results demonstrate that, for the sulfur positive electrode, sulfur is reduced to form aluminum sulfide in the discharge process, and then oxidized to sulfur in the subsequent charge process. The electrochemical reaction mechanism can be described by the following equations:

Positive electrode: $8\text{Al}_2\text{Cl}_7^- + 6\text{e}^- + 3\text{S} \rightleftharpoons \text{Al}_2\text{S}_3 + 14\text{AlCl}_4^-$ (1)

Negative electrode: $2\text{Al} + 14\text{AlCl}_4^- \rightleftharpoons 8\text{Al}_2\text{Cl}_7^- + 6\text{e}^-$ (2)

Overall reaction: $3\text{S} + 2\text{Al} \rightleftharpoons \text{Al}_2\text{S}_3$ (3)

2.3 The electrocatalytic effect of CoNG on the sulfur conversion

Based on the above reaction mechanism and previous works on Al-S batteries, the electrochemical conversion of sulfur and aluminum sulfide would undergo high kinetics energy barrier, ascribing to the insulating nature of sulfur, the tough release of Al^{3+} from Al_2Cl_7^- , and the difficulties in breaking three robust Al-S bonds (332 kJ mol^{-1} for Al-S single bond).⁴⁴ The sluggish kinetics leads to a high charge-discharge voltage gap, which is usually higher than 0.6 V in the previous reports.^{9,14,15} Apparently, the voltage gap is as low as 0.43 V in our quasi-solid-state Al-S battery, which could be related to the CoNG host. To figure out the functional mechanism of CoNG host, a series of contrast samples are synthesized for comparison, including graphene (G), nitrogen doped graphene (NG) and cobalt decorated graphene (CoG), which are further used as sulfur host to form S@G, S@NG and S@CoG, respectively.

Similar to CoNG, these contrast samples also present a sheet-like structure (**Figure S12a-c**). Particularly, many small particles are found on the graphene sheet in CoG sample (**Figure S12c**). After loading sulfur, these materials remain intact sheet structure and sulfur is distributed on their graphene surfaces (**Figure S12d-f**). The XRD results further confirm that sulfur is successfully loaded onto these carbon host (**Figure S13a**). Note that the Co diffraction peak exists in CoG and S@CoG samples, indicating that these small particles distributed on the graphene are elemental cobalt. To remove redundant Co particles, the CoNG is treated by acid soaking during the synthesis process. Obviously, after acid treatment, no elemental Co remains in the CoNG sample (**Figure S13b**), which is consistent with the XPS results (Figure 2e). All CoNG samples used in this work are obtained with the above method.

Figure 3a shows the charge/discharge profiles of liquid-state Al-S batteries assembled by S@G, S@NG, S@CoG and S@CoNG positive electrodes, respectively. It is clear that the discharge capacities are in the order of $\text{S@CoNG} > \text{S@NG} > \text{S@CoG} > \text{S@G}$. Moreover, the discharge voltage and voltage hysteresis (ΔE) of these batteries are compared (**Figure S14**), among which S@CoNG exhibits the highest discharge voltage of 0.98 V. Meanwhile, the largest voltage hysteresis of 1.2 V is obtained for S@G, whereas a significant reduction of the voltage hysteresis is observed in the nitrogen (and cobalt)-doped or cobalt-decorated graphene samples. In particular, the S@CoNG-based Al-S battery possesses the smallest voltage hysteresis of 0.32 V, which is superior to that of all previous reports.^{8-11, 14,15} Obviously, the improved electrochemical performance of S@CoNG was derived from the CoNG host, which may be beneficial to accelerate the entire reaction kinetics. To further evaluate the effects of CoNG on the electrochemical conversion of sulfur, half cells and symmetric cells are assembled with these four types of hosts as electrode, respectively. CV curves are conducted on half cells with host materials as working

electrodes and Al foil as counter electrodes in the IL electrolyte containing sulfur (S+IL), as shown in Figure 3b. Each CV curve exhibits a pair of redox peaks, which is agreement with the CV results of the Al-S batteries with four sulfur-based positive electrodes (**Figure S15**), indicating that the pair of redox peaks correspond to the reduction of sulfur and the oxidation of aluminum sulfide. Note that the reduction peak for CoNG shows the most positive potential and the largest peak current among these four host materials, further confirming that CoNG could promote the reduction kinetics of sulfur. Figure 3c presents the CV curves of symmetric cells with identical working and counter electrodes in the IL electrolyte containing sulfur and aluminum sulfide (S+Al₂S₃+IL). The CV curve of CoNG exhibits a pair of reduction/oxidation peaks located at -0.44 V (Peak A) and 0.45 V (Peak B). Peak A in the cathodic scan arises from the reduction of sulfur on the working electrode and oxidation of aluminum sulfide on the counter electrode, and peak B is due to the oxidation of aluminum sulfide to generate sulfur on the working electrode.^{14,47} The CV curves of NG and CoG also show a pair of redox peaks, but the potential difference between the cathodic and anodic peaks is much higher than that of GoNG, and the CV peaks are barely visible for G electrodes. Furthermore, Tafel plots have been derived to analyze the effect of four graphene-based materials on redox reaction kinetics of sulfur (Figure 3d). Obviously, GoNG shows the lowest Tafel slope of 219 mV dec⁻¹ for the sulfur reduction and 173 mV dec⁻¹ for sulfide oxidation among the four host materials, indicating the accelerated sulfur conversion. Meanwhile, exchange current densities (j_0) were calculated from the Tafel plots, which reflect the intrinsic electron transfer rate of reaction (**Table S3**). The CoNG electrode shows the largest exchange current densities for both the cathodic process and the anodic process, which are 4.12 and 0.19 mA cm⁻², compared to those of the G (1.39 and 0.01 mA cm⁻²), NG (1.98 and 0.02 mA cm⁻²) and CoG (2.63 and 0.09 mA cm⁻²). Thus, the increase of exchange current density values clearly validates more faster charge transfer induced by CoNG in both charge and discharge processes. Note that these four host materials possess similar graphene-like morphology except different heteroatoms doping, and the reaction kinetics of sulfur conversion on CoNG is the fastest. Therefore, the Co-N center in CoNG should be the major reason responsible for the improved electrochemical performance.

To verify the effect of Co-N structure on sulfur conversion, the evolution of chemical states for Co and N in S@CoNG-based Al-S batteries are studied by *ex-situ* XPS. In the N signal of pristine sample, there are three peaks assigned to pyridinic-N (Py N), Co-N and graphitic-N (Gr N), respectively (Figure 3e). In the case of the charging/discharging intermediate products (discharge to 0.8 V and charge to 1.3 V, as abbreviated to D-0.8V and C-1.3V, respectively), a new peak (400.5 eV) ascribed to the Co-N-Al signal is found, indicating that the Co-N structures interact with the aluminum-based cluster (Al_xCl_y and Al_xS_y) during cycling.⁵⁴ Likewise, compared with the Co signal of the pristine sample, the intermediate product also presents a new peak (778.8 eV) allocated to S-Co-N (Figure 3f), suggesting the interaction between the Co-N structure and sulfur-based compounds (Al_xS_y) in the charge and discharge processes.¹⁴ Based on the above XPS results, we speculate that the Co-N center could catalyze the breaking of the Al-Cl and S-S bonds during the discharge process and the breaking of the Al-S bond during the charge process.

To further understand the catalytic mechanism of Co-N structure on the electrochemical reaction, the first-principles calculations are performed to investigate the possible reactions from sulfur to aluminum sulfide in the four host materials. Based on above Raman results (Figure 2l), the models of four graphene-based hosts and various reaction primitives are considered (Figure S16), and the electrochemical reduction reaction of sulfur is illustrated in Figure 3g, including dissociation of Al^{3+} from Al_2Cl_7^- and transformation from S to Al_2S_3 . Firstly, the Al^{3+} release pathways are investigated, and the first step involves decomposition of Al_2Cl_7^- to form AlCl_4^- , which is stepwise dissociated into AlCl_2^+ , AlCl^{2+} , and end product Al^{3+} (Figure S17). The Gibbs free energies are calculated for the above reactions on the four graphene-based substrates (Figure 3h and Table S4). It is clear that all reactions are unspontaneous, and the formation of AlCl_2^+ from AlCl_4^- has the largest positive Gibbs free energy (ΔG_2), indicating that this is the rate-limiting step in the whole process. This value is 1.22 eV for CoNG, which is lower than that of G (1.69 eV), NG (1.55 eV) and CoG (1.41 eV), manifesting that the formation of Al^{3+} is thermodynamically most favorable on CoNG substrate. During the subsequent S reduction process, the S_8 couples with Al^{3+} ions and undergoes further reduction with the stepwise formation of Al_2S_{18} , Al_2S_{12} , Al_2S_6 , and end product Al_2S_3 (Figure S18 and Table S5).⁵⁵ Note that after the spontaneous exothermic conversion from S_8 to Al_2S_{18} , the subsequent three steps to form Al_2S_{12} , Al_2S_6 , and Al_2S_3 are either endothermic or nearly thermoneutral (Figure 3i). Obviously, the formation of Al_2S_3 from Al_2S_6 has the largest positive Gibbs free energy (ΔG_4), corresponding to the rate-limiting step in this process. Likewise, the energy barrier of this process on CoNG (2.25 eV) is the lowest among the four host materials (3.62 eV on G, 3.03 eV on NG and 2.70 eV on CoG), clearly confirming that Co-N structure in CoNG serves as catalytic sites to accelerate Al_2S_3 formation. To further reveal how the CoNG accelerate the two rate-limiting steps, the electron distribution is simulated to evaluate the charge transfer process. During the dissociation of AlCl_4^- into AlCl_2^+ on CoNG, the Bader charge of Co atoms and N atoms significantly increases from 8.0 to 8.6 and from 6 to 6.5 respectively, along with an unchanged state for Al and Cl atoms (Figure 3j, k), suggesting that the Co-N structure loots the charge from Al atoms and eventually breaks the Al-Cl bonds. For the formation of Al_2S_3 from Al_2S_6 on CoNG, the Bader charge of S increases from 6.5 to 7.2 and the charge of Co decreases from 8.0 to 7.1 (Figure 3l, m), indicating that Co atoms donate electrons to S atoms and cause the breaking of S-S and S-Al bonds. The theoretical calculation results confirm that the Co-N structure acts as the active center to induce the breaking of Al-Cl and S-S bonds, thus accelerating the kinetics of sulfur reduction reaction.

2.4 The electrochemical performance and restriction on polysulfide of IL@MOF quasi-solid-state electrolyte

The porous zirconium-based MOF was selected as the host for impregnation of IL to construct IL@MOF quasi-solid-state electrolyte. The BET surface area of the MOF is $1611 \text{ m}^2 \text{ g}^{-1}$ and the dominating pore sizes are 0.98 nm and 1.25 nm according to the N_2 adsorption/desorption isothermal tests (Figure S19a, b). The size of IL ions (AlCl_4^- , Al_2Cl_7^- , and EMI^+) have been calculated to be less than 0.8 nm in the

longest dimension, so the porous MOF can load a large amount of IL and allow IL ions to pass through.⁵⁶ After IL impregnating, the BET surface area sharply declines to only $18.6 \text{ m}^2 \text{ g}^{-1}$ and the pore size distribution is almost nonexistent for IL@MOF composite (**Figure S19c, d**), indicating that the pores of the MOF have been almost filled up with IL ions. Meanwhile, for IL@MOF, the characteristic XRD peaks of MOF become weak and most of them disappear as reported in previous works (**Figure S20**),⁵⁷ further confirming the successful impregnation of IL. The SEM images show that the synthesized IL@MOF crystals are regular polyhedron with a particle size of about 200~300 nm (Figure 4a), and plentiful Al elements are detected in IL@MOF (**Figure S21**), indicating the uniform distribution of chloroaluminate-based ions in MOF. The IL@MOF particles are pressed into circular pellet (inset in Figure 4a) for further testing.

High ionic conductivities of 4.2×10^{-4} and $2.5 \times 10^{-3} \text{ S cm}^{-1}$ for IL@MOF are observed at 20 and 100°C (Figure 4b), respectively, indicating a fast ion migration under a wide temperature range. Meanwhile, the activation energy (E_a) of IL@MOF is evaluated to be 233 meV (**Figure S22**), manifesting an efficient ion transport. Apparently, the high ionic mobility of IL@MOF is derived from IL ions, since the MOF is an ionic insulator and merely serves as a porous framework to enable rapid IL ions movement.⁵⁸ Furthermore, the IL@MOF electrolyte can achieve reversible deposition and stripping of aluminum with a small polarization potential (**Figure S23**), demonstrating free movement of chloroaluminate-based ions (Al_2Cl_7^- and AlCl_4^-). The interface features between IL@MOF electrolyte and Al metal are evaluated by the direct current Al plating/stripping cycles, as shown in Figure 4c. A large polarization voltage of $\pm 98 \text{ mV}$ is observed in the initial cycle at 0.05 mA cm^{-2} , indicating a high interfacial impedance between IL@MOF and Al metal. During subsequent cycles, the polarization voltage decreases and stabilizes at 71 mV, and it remains at 83 mV over 200 h at a higher current density of 0.1 mA cm^{-2} (**Figure S24**), representing the formation of a stable IL@MOF/Al interface layer with high ion transport. The above results demonstrate that the IL@MOF electrolyte possesses high active ion transport and can establish a stable interface layer with Al metal for long-time cycling, meeting the requirements for high-performance Al-S batteries.

Sulfur, polysulfide and aluminum sulfide could dissolve in IL electrolyte to some extent^{10,15}. In the liquid-state Al-S battery after 20 cycles, black substance can be clearly seen on both the conventional separator (GF/A) and Al foil (**Figure S25**). The black substance is detected by XPS and proved to be sulfur and aluminum compounds, which must have originated from the sulfur positive electrode. This result indicates that sulfur and intermedium will pass through the separator and deposit on the Al negative electrode during the cycling, which is responsible for the poor cycle stability of liquid-state Al-S battery (Figure 1e). The IL@MOF electrolyte is used in this work to inhibit the shuttle effect of these active substances. To verify the suppression of sulfur-based compound diffusion, permeation experiments are conducted using H-type cell for visualization, in which the IL electrolyte with dissolved S and Al_2S_3 (left chamber) and blank IL electrolyte (right chamber) are separated by the GF/A separator and IL@MOF pellet, respectively. As illustrated in Figure 4d, the solution in right chamber gradually darkens when routine GF/A separator is used. For the case of IL@MOF, no visible change in color of blank electrolyte is

found even after 48 hours, indicating the effective inhibition of the shuttle effect. After permeation experiment, the solution in right chamber is further monitored with Fourier transform infrared spectroscopy (FTIR). The sulfur signal is clearly observed in the solution when GF/A separator is used, but is not found when using IL@MOF (Figure 4e), suggesting that S and Al_2S_3 could not travel through the IL@MOF. Apparently, polysulfides with larger sizes are also unable to pass through the IL@MOF in quasi-solid-state Al-S batteries, fundamentally addressing the issue of shuttle effect. To further evaluate the inhibition ability of IL@MOF toward these sulfur-based compounds, element information at three different points inside cycled quasi-solid-state Al-S battery is detected, as shown in Figure 4f and 4g. The S and S^{x-} (Al_2S_x and Al_2S_3) signal are obviously detected in point 1 (in the composite positive electrode) and point 2 (the interface between positive electrode and IL@MOF electrolyte), but there is no sulfur signal at point 3 (in the middle of the IL@MOF electrolyte), further confirming the effective suppression of polysulfide diffusion. For IL@MOF, the narrow pore of MOF (size: ~ 1.2 nm) is filled up with the chloroaluminate-based IL ions, which effectively inhibits the shuttle effect of soluble sulfur compounds, achieving an excellent cycle stability of quasi-solid-state Al-S batteries.

3. Discussion

The Al-S batteries suffer from the high voltage hysteresis and fast capacity decay due to the sluggish kinetics of sulfur conversion and shuttle effect of soluble polysulfide. Through understanding the sulfur conversion kinetics in the present work, utilization of CoNG as electrocatalyst accelerates the kinetics of sulfur, endowing the Al-S batteries with small voltage gap and favorable discharge potential. Meanwhile, encapsulating IL into MOF to fabricate quasi-solid-state electrolyte significantly inhibit the shuttle effect of soluble sulfide, realizing a long-term stable quasi-solid-state Al-S battery. Nevertheless, there is still a lot of room for further improving the overall battery performance, including unsatisfactory rate capacity (Figure 1d), low Coulombic efficiency and sulfur utilization (Figure 1e), by increasing the doped catalytic structure in graphene and enhancing the ion transport in quasi-solid-state electrolyte. Considering the catalytic mechanism of CoNG, other similar types of electrocatalysts, including Fe-N co-doped graphene (Figure S26), Ni-N co-doped graphene, and Pt decorated graphene, would be the promising sulfur-host candidates for advanced Al-S batteries. In addition, for the IL@MOF electrolyte, the porosity and pore structure of MOF could be further modified for elevating active ion transport. Apparently, owing to the similar issue in other prototypes of sulfur-based batteries (*e.g.*, Li-S batteries, Na-S batteries, and Mg-S batteries), the design strategies here could be well extended to substantially reduce voltage hysteresis and alleviate capacity decay, aiming to achieve high-performance sulfur-based batteries.

4. Conclusion

In summary, the first prototype of quasi-solid-state Al-S batteries are demonstrated for fundamentally addressing the issues of large voltage gap and rapid capacity decay in Al-S batteries. For tackling the sluggish kinetics of sulfur conversion, a CoNG electrocatalyst is employed as the sulfur host to greatly accelerate reaction kinetics. Consequently, the electrocatalyst-boosting Al-S batteries present a low

voltage hysteresis of 0.32 V, along with a high discharge plateau of 0.98 V. Meanwhile, the utilization of IL@MOF quasi-solid-state electrolyte constructed by encapsulating IL into MOF effectively inhibits the shuttle effect of polysulfides. As a result, the quasi-solid-state Al-S batteries could still deliver a high specific capacity of 820 mAh g⁻¹ with 78% capacity retention beyond 300 cycles, revealing a long-term life span. More importantly, the design principle here endows the Al-S batteries with good rechargeable ability, which could be extended to other sulfur-based batteries, providing a feasible strategy to promote the development of energy storage technology.

5. Methods

Synthesis of doped graphene-based materials

100 mg of graphene oxide (GO) and 1 g of urea was sequentially dispersed in 100 mL of deionized water under sonication to form homogeneous dispersion. 20 mg CoCl₂·6H₂O was added into the above solution followed by further sonication. The mixed solution was freeze-dried and then annealed at 900°C under Ar for achieving Co/N doping and GO reduction to obtain black powders. The black powder was soaked in 0.1 M HCl to remove redundant Co simple substance and was dried in vacuum to obtain CoNG. The G, NG, and CoG was synthesized with above method except without adding urea and CoCl₂·6H₂O, CoCl₂·6H₂O, and urea, respectively, and without acid soaking. Additionally, the FeNG was synthesized in a similar way using FeCl₂·4H₂O as the Fe source.

Synthesis of sulfur@graphene-based composites

120 mg of sulfur powder was first dissolved in 2 mL of CS₂. Then, 50 mg of prepared graphene-based material (G, NG, CoG, CoNG, and FeNG) was added to the solution and allowed CS₂ evaporation under stirring at room temperature. The mixture was then transferred into a Teflon reactor and heated at 155°C for 10 h to yield the sulfur-embedded composites (S@G, S@NG, S@CoG, S@CoNG, and S@FeNG).

Synthesis of IL@MOF electrolyte: The anhydrous AlCl₃ and 1-ethyl-3-methylimidazoliumchloride ([EMIm]Cl) with a molar ratio of 1.3:1 was slowly mixed and dissolved to obtain the light-yellow IL electrolyte, which was further stirred in glove box for 24 h before use. Terephthalic acid (BDC) and ZrCl₄ with a molar ratio of 1:1 was successively dissolved in N, N-dimethylformamide (DMF) under stirring into a homogeneous solution. This solution was transferred into an autoclave and heated at 120°C for 24 h. The precipitation was collected by centrifuging and washing with methanol and then activated by heating at 120°C in dynamic vacuum to obtain Zr-MOF. An amount of IL was added to the activated MOF and further milled into homogeneous mixture in glove box, and then the mixture was heated at 120°C in the vacuum overnight to obtain IL@MOF electrolyte.

Assembly of Al-S battery: The liquid-state Al-S batteries were assembled using pouch cells with sulfur positive electrode, IL electrolyte, glass fiber (GF/A) separator and Al negative electrode. The positive electrode was prepared by mixing sulfur composite powders (S@G, S@NG, S@CoG, S@CoNG, and

S@FeNG), acetylene black, and polyvinylidene fluoride (PVDF) with mass ratio of 8:1:1 and dissolving in N-methyl-2-pyrrolidone (NMP) to form homogeneous slurry, which was then coated on a Ta foil (the diameter of 12 mm) current collector with a metallic Mo tab. The average loading of active materials was around 2 mg cm^{-2} . The quasi-solid-state Al-S batteries were assembled using Swagelok cells. The S@CoNG, IL@MOF, and acetylene black were mixed in various mass ratio and pressed into a diameter of 10 mm pellet under 3 MPa force, and then further pressed with another 20 mg IL@MOF and Al foil with $50 \mu\text{m}$ thickness into a diameter of 15 mm three layers pellet under 5 MPa force in glove box. Then the three layers pellet were put into a Swagelok cell with Mo rod as current collector. The active materials have a loading of 3.0 mg cm^{-2} .

Electrochemical measurements

Half cells were assembled with Al foil and work electrodes that consisted of a mixture of 80 wt % of the active material (G, NG, CoG, CoNG, and FeNG) and 20 wt% of PVDF. The electrolyte was sulfur saturated ionic liquids (S+IL). Cyclic voltammetry (CV) was performed between 0.1 and 2.0 V at the scan rate of 0.5 mV s^{-1} . Symmetric cells were assembled with two same electrodes as described above. The electrolyte was sulfur and aluminum sulfide saturated ionic liquids (S+Al₂S₃+IL). CV was performed between -2.0 and 2.0 V at the scan rate of 1 mV s^{-1} . 20 mg IL@MOF was pressed into a diameter of 15 mm pellet under 5 MPa force and assembled into Mo|IL@MOF|Mo, Al|IL@MOF|Mo, and Al|IL@MOF|Al Swagelok cells for the test of the ionic conductivity and Al plating/stripping. All electrochemical impedance spectroscopy (EIS) and CV were carried out with a CHI 660E electrochemical workstation. The galvanostatic charge/discharge of all batteries were performed with a Neware battery testing system in the voltage range of 0.1–1.8 V. The activation energy (E_a) of the IL@MOF electrolyte was calculated according to the Arrhenius equation

$$\sigma = \sigma_0 \exp(-E_a/kT)$$

where, σ is the ionic conductivity, σ_0 is the pre-exponential factor, k is the Boltzmann constant, and T is the temperature.

Characterizations

The crystal structures of the as-prepared materials were characterized by X-rays diffraction (XRD, Rigaku, Cu K α wave). The morphologies of materials were examined by scanning electron microscope (SEM, HITACHI, S-4800) and transmission electron microscope (TEM, JEOL, JSM2100F). The sulfur loading of the composite was determined by thermogravimetric analysis (TGA, STA449F3) in the temperature range of 20–500 °C under N₂ atmosphere. The specific surface area and size distributions of MOF and IL@MOF were estimated by Barrett–Joyner–Halenda (BJH) methods. The composition in IL electrolyte after penetration test was measured by Raman spectroscopy (HORIBA, $\lambda = 473 \text{ nm}$). The elemental valence of CoNG and S@CoNG electrode with different discharge depths were characterized by X-ray photoelectron spectroscopy (XPS, Kratos Ltd) and Raman (HORIBA, $\lambda = 633 \text{ nm}$). Co K-edge spectra were

obtained under ambient conditions at 4B9A beamline of the Beijing Synchrotron Radiation Facility, and all X-ray absorption spectroscopy (XAS) spectra were normalized using Athena software.

Calculation

All calculations were performed in Vienna ab-initio simulation package (VASP) using density functional theory (DFT) method. The projector augmented wave (PAW) method was used to describe electron-ion interactions. The generalized gradient approximation (GGA) with the Perdew–Burke–Ernzerhof (PBE) functional was adopted to describe electron exchange and correlation energy. A supercell of graphene containing 6×6 unit cells was used to all graphene-based systems. The first Brillouin zone was sampled with a k-points mesh of 3×3×3 Gamma-centered grids for geometric optimization. The total energy convergence was set to be lower than 1×10^{-5} eV, with the force convergence set at 0.01 eV/Å. A cutoff energy of 520 eV was used for the plane waves in all calculations. The choice of these computational parameters ensured good convergence in this work.

Declarations

Acknowledgements

This work was supported by National Natural Science Foundation of China (Nos. 51725401 and 51874019).

Author contributions

S. J. and D. F. conceived the concept. S. J., W. W., and W. -L. S. designed the experiments. Z. H. carried out the experiments. W. W. and Z. H. co-wrote the manuscript. M. W. and H. C. participated in characterizations and result analysis. All authors discussed the results.

Competing interests

The authors declare no conflict of interest.

References

1. Dunn, B., Kamath, H., & Tarascon, J. M. Electrical energy storage for the grid: a battery of choices. *Science* **334**, 928–935 (2011).
2. Liang, Y., Dong, H., Aurbach, D. & Yao, Y. Current status and future directions of multivalent metal-ion batteries. *Nat. Energy* **5**, 646–656 (2020).
3. Elia, G. A. *et al.* An overview and future perspectives of aluminum batteries. *Adv. Mater.* **28**, 7564–7579 (2016).
4. Tu, J. *et al.* Nonaqueous rechargeable aluminum batteries: progresses, challenges, and perspectives. *Chem. Rev.* **121**, 4903–4961 (2021).

5. Wu, F., Yang, H., Bai, Y. & Wu, C. Paving the path toward reliable cathode materials for aluminum-ion batteries. *Adv. Mater.* **31**, 1806510 (2019).
6. Faegh, E., Ng, B., Hayman, D. & Mustain, W. E. Practical assessment of the performance of aluminium battery technologies. *Nat. Energy* **6**, 21–29 (2020).
7. Yang, H. *et al.* The rechargeable aluminum battery: opportunities and challenges. *Angew. Chem. Int. Ed.* **58**, 11978–11996 (2019).
8. Cohn, G., Ma, L. & Archer, L. A. A novel non-aqueous aluminum sulfur battery. *J. Power Sources* **283**, 416–422 (2015).
9. Gao, T. *et al.* A rechargeable Al/S battery with an ionic-liquid electrolyte. *Angew. Chem. Int. Ed.* **55**, 9898–9901 (2016).
10. Yu, X. & Manthiram, A. Electrochemical energy storage with a reversible nonaqueous room-temperature aluminum–sulfur chemistry. *Adv. Energy Mater.* **7**, 1700561 (2017).
11. Yu, X., Boyer, M. J., Hwang, G. S. & Manthiram, A. Room-temperature aluminum-sulfur batteries with a lithium-ion-mediated ionic liquid electrolyte. *Chem* **4**, 586–598 (2018).
12. Bian, Y. *et al.* Using an AlCl₃/urea ionic liquid analog electrolyte for improving the lifetime of aluminum-sulfur batteries. *ChemElectroChem* **5**, 3607–3611 (2018).
13. Li, H. *et al.* Reversible electrochemical oxidation of sulfur in ionic liquid for high-voltage Al-S batteries. *Nat. Commun.* **12**, 5714 (2021).
14. Guo, Y. *et al.* Rechargeable aluminium-sulfur battery with improved electrochemical performance by cobalt-containing electrocatalyst. *Angew. Chem. Int. Ed.* **59**, 22963–22967 (2020).
15. Guo, Y. *et al.* Carbonized-MOF as a sulfur host for aluminum-sulfur batteries with enhanced capacity and cycling life. *Adv. Funct. Mater.* **29**, 1807676 (2019).
16. Yang, H. *et al.* An aluminum-sulfur battery with a fast kinetic response. *Angew. Chem. Int. Ed.* **57**, 1898–1902 (2018).
17. Bhauriyal, P., Das, S. & Pathak, B. Theoretical insights into the charge and discharge processes in aluminum–sulfur batteries. *J. Phys. Chem. C* **124**, 11317–11324 (2020).
18. Pan, H., Cheng, Z., He, P. & Zhou, H. A review of solid-state lithium–sulfur battery: ion transport and polysulfide chemistry. *Energy & Fuels* **34**, 11942–11961 (2020).
19. Li, M. *et al.* Solid-state lithium–sulfur battery enabled by thio-LiSICON/polymer composite electrolyte and sulfurized polyacrylonitrile cathode. *Adv. Funct. Mater.* **30**, 1910123 (2020).
20. Zhou, D. *et al.* A stable quasi-solid-state sodium-sulfur battery. *Angew. Chem. Int. Ed.* **57**, 10168–10172 (2018).
21. Yue, J. *et al.* High-performance all-inorganic solid-state sodium-sulfur battery. *ACS Nano* **11**, 4885–4891 (2017).
22. Ye, C. *et al.* Electron-state confinement of polysulfides for highly stable sodium-sulfur batteries. *Adv. Mater.* **32**, 1907557 (2020).
23. Ding, J. *et al.* Review of emerging potassium-sulfur batteries. *Adv. Mater.* **32**, 1908007 (2020).

24. Ye, C. *et al.* Catalytic oxidation of K_2S via atomic Co and pyridinic N synergy in potassium-sulfur batteries. *J. Am. Chem. Soc.* **143**, 16902–16907 (2021).
25. Wang, P., Buchmeiser, M. R. Rechargeable magnesium–sulfur battery technology: state of the art and key challenges. *Adv. Funct. Mater.* **29**, 1905248 (2019).
26. Shao, M., Chang, Q., Dodelet, J. P. & Chenitz, R. Recent advances in electrocatalysts for oxygen reduction reaction. *Chem. Rev.* **116**, 3594–3657 (2016).
27. Wang, D.-W. & Su, D. Heterogeneous nanocarbon materials for oxygen reduction reaction. *Energy Environ. Sci.* **7**, 576–591 (2014).
28. Dai, L., Xue, Y., Qu, L., Choi, H. J. & Baek, J. B. Metal-free catalysts for oxygen reduction reaction. *Chem. Rev.* **115**, 4823–4892 (2015).
29. Suen, N. T. *et al.* Electrocatalysis for the oxygen evolution reaction: recent development and future perspectives. *Chem. Soc. Rev.* **46**, 337–365 (2017).
30. Zhou, X., Huang, J., Pan, Z. & Ouyang, M. Impedance characterization of lithium-ion batteries aging under high-temperature cycling: importance of electrolyte-phase diffusion. *J. Power Sources* **426**, 216–222 (2019).
31. Sun, H. *et al.* A new aluminium-ion battery with high voltage, high safety and low cost. *Chem. Commun.* **51**, 11892–11895 (2015).
32. Lin, M. C. *et al.* An ultrafast rechargeable aluminium-ion battery. *Nature* **520**, 325–328 (2015).
33. Jayaprakash, N., Das, S. K. & Archer, L. A. The rechargeable aluminum-ion battery. *Chem. Commun.* **47**, 12610–12612 (2011).
34. Liu, J., Li, Z., Huo, X. & Li, J. Nanosphere-rod-like Co_3O_4 as high performance cathode material for aluminium ion batteries. *J. Power Sources* **422**, 49–56 (2019).
35. Wang, S. *et al.* High-performance aluminum-ion battery with $CuS@C$ microsphere composite cathode. *ACS Nano* **11**, 469–477 (2017).
36. Mori, T. *et al.* Discharge/charge reaction mechanisms of FeS_2 cathode material for aluminum rechargeable batteries at 55°C. *J. Power Sources* **313**, 9–14 (2016).
37. Li, G., Tu, J., Wang, M. & Jiao, S. Cu_3P as a novel cathode material for rechargeable aluminum-ion batteries. *J. Mater. Chem. A* **7**, 8368–8375 (2019).
38. Kim, D. J. *et al.* Rechargeable aluminium organic batteries. *Nat. Energy* **4**, 51–59 (2018).
39. Bitenc, J. *et al.* Concept and electrochemical mechanism of an Al metal anode–organic cathode battery. *Energy Storage Mater.* **24**, 379–383 (2020).
40. Raju, V., Rani, J. V. & Basak, P. Self-arranged polythiophene on multi-walled carbon nanotube templated composites: synthesis and application in rechargeable aluminium battery. *Electrochim. Acta* **361**, 137091 (2020).
41. Wang, S., Huang, S., Yao, M., Zhang, Y. & Niu, Z. Engineering active sites of polyaniline for $AlCl_2^{(+)}$ storage in an aluminum-ion battery. *Angew. Chem. Int. Ed.* **59**, 11800–11807 (2020).

42. Ha, Y. *et al.* Atomically dispersed Co-pyridinic N-C for superior oxygen reduction reaction. *Adv. Energy Mater.* **10**, 2002592 (2020).
43. Li, Y. *et al.* A freestanding flexible single-atom cobalt-based multifunctional interlayer toward reversible and durable lithium-sulfur batteries. *Small Methods* **4**, 1900701 (2020).
44. Liang, Z. *et al.* Cobalt-nitrogen-doped helical carbonaceous nanotubes as a class of efficient electrocatalysts for the oxygen reduction reaction. *Angew. Chem. Int. Ed.* **57**, 13187–13191 (2018).
45. Shang, L. *et al.* Well-dispersed ZIF-derived Co,N-Co-doped carbon nanoframes through mesoporous-silica-protected calcination as efficient oxygen reduction electrocatalysts. *Adv. Mater.* **28**, 1668–1674 (2016).
46. Zhu Y, Zhang Z, Lei Z, *et al.* Defect-enriched hollow porous Co–N-doped carbon for oxygen reduction reaction and Zn-Air batteries. *Carbon*, **167**, 188–195 (2020).
47. Du, Z. *et al.* Cobalt in Nitrogen-doped graphene as single-atom catalyst for high-sulfur content lithium-sulfur batteries. *J. Am. Chem. Soc.* **141**, 3977–3985 (2019).
48. Funke, H., Scheinost, A. C. & Chukalina, M. Wavelet analysis of extended X-ray absorption fine structure data. *Phys. Rev. B* **71**, 094110 (2005).
49. Zhou G, Yin L C, Wang D W, *et al.* Fibrous hybrid of graphene and sulfur nanocrystals for high-performance lithium–sulfur batteries. *ACS Nano*, **7**, 5367–5375 (2013).
50. Chen, W. *et al.* A new hydrophilic binder enabling strongly anchoring polysulfides for high-performance sulfur electrodes in lithium-sulfur battery. *Adv. Energy Mater.* **8**, 1702889 (2018).
51. Song, Y.-X. *et al.* Direct tracking of the polysulfide shuttling and interfacial evolution in all-solid-state lithium–sulfur batteries: a degradation mechanism study. *Energy Environ. Sci.* **12**, 2496–2506 (2019).
52. Hagen, M. *et al.* In-situ Raman investigation of polysulfide formation in Li-S Cells. *J. Electrochem. Soc.* **160**, 1205–1214 (2013).
53. Zhu, W. *et al.* Investigation of the reaction mechanism of lithium sulfur batteries in different electrolyte systems by in situ Raman spectroscopy and in situ X-ray diffraction. *Sustain. Energy & Fuels* **1**, 737–747 (2017).
54. Zhang, L. *et al.* Single nickel atoms on nitrogen-doped graphene enabling enhanced kinetics of lithium-sulfur batteries. *Adv. Mater.* **31**, 1903955 (2019).
55. Xiao, X., Tu, J., Huang, Z. & Jiao, S. A cobalt-based metal-organic framework and its derived material as sulfur hosts for aluminum-sulfur batteries with the chemical anchoring effect. *Phys. Chem. Chem. Phys.* **23**, 10326–10334 (2021).
56. Zhang, H., Cao, G., Yang, Y. & Gu, Z. Capacitive performance of an ultralong aligned carbon nanotube electrode in an ionic liquid at 60°C. *Carbon* **46**, 30–34 (2008).
57. Fujie, K., Otsubo, K., Ikeda, R., Yamada, T. & Kitagawa, H. Low temperature ionic conductor: ionic liquid incorporated within a metal-organic framework. *Chem. Sci.* **6**, 4306–4310 (2015).

58. Wu, J. F. & Guo, X. Nanostructured metal-organic framework (MOF)-derived solid electrolytes realizing fast lithium ion transportation kinetics in solid-state batteries. *Small* **15**, 1804413 (2019).

Figures

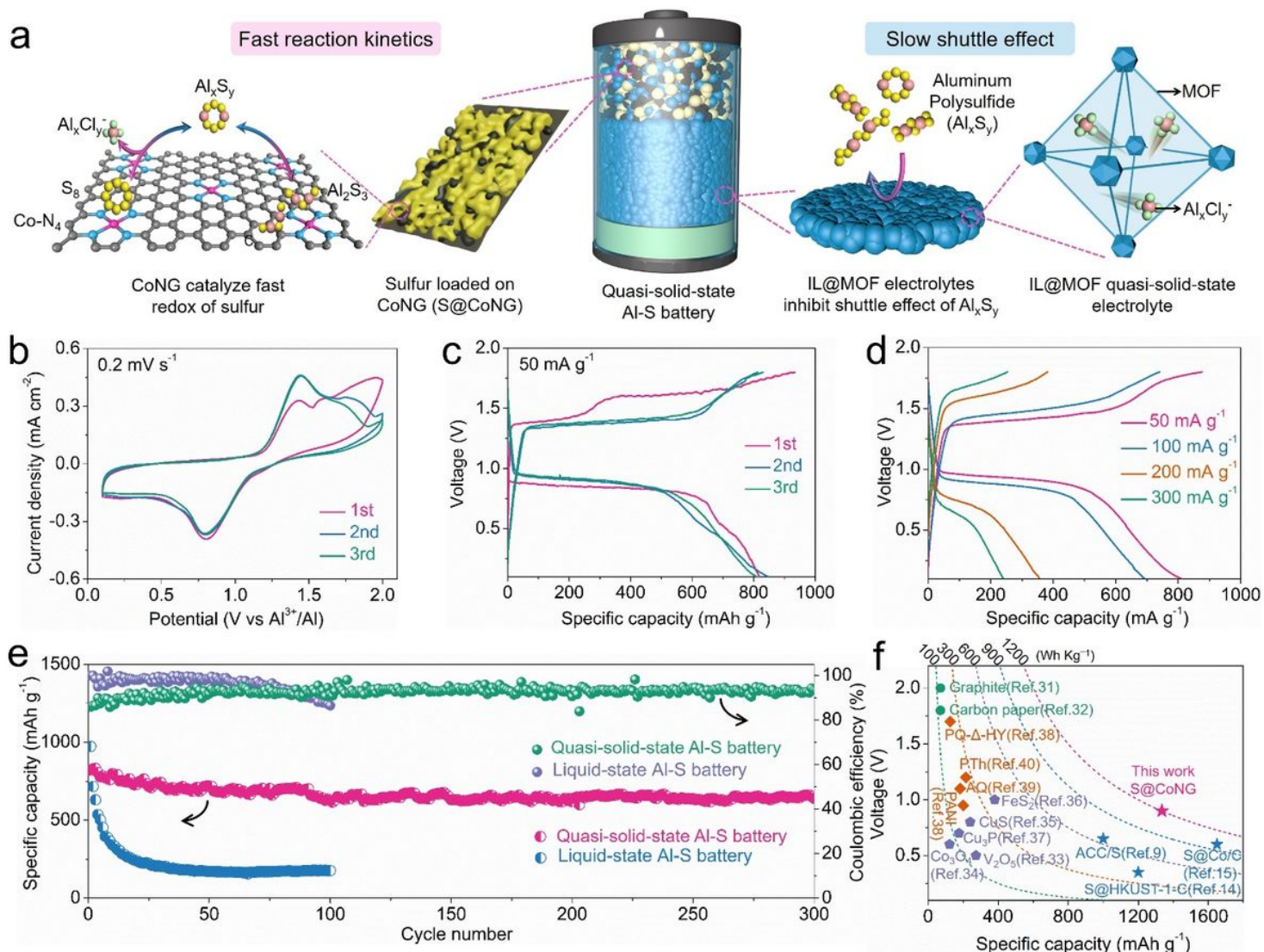


Figure 1

The construction and electrochemical performance of quasi-solid-state Al-S batteries. (a) Schematic illustration of the quasi-solid-state Al-S battery and its working mechanism. (b) CV curves of the Al|IL@MOF|S@CoNG battery in the voltage range of 0.1–2.0 V. (c) The charge and discharge curves of Al|IL@MOF|S@CoNG battery at a current density of 50 mA h g^{-1} . (d) The charge/discharge profiles of the Al|IL@MOF|S@CoNG batteries at different current density. (e) Cyclic stability test of the liquid-state and quasi-solid-state Al-S battery at 50 mA g^{-1} . (f) Performance comparison of our quasi-solid-state Al-S battery with other Al battery systems.

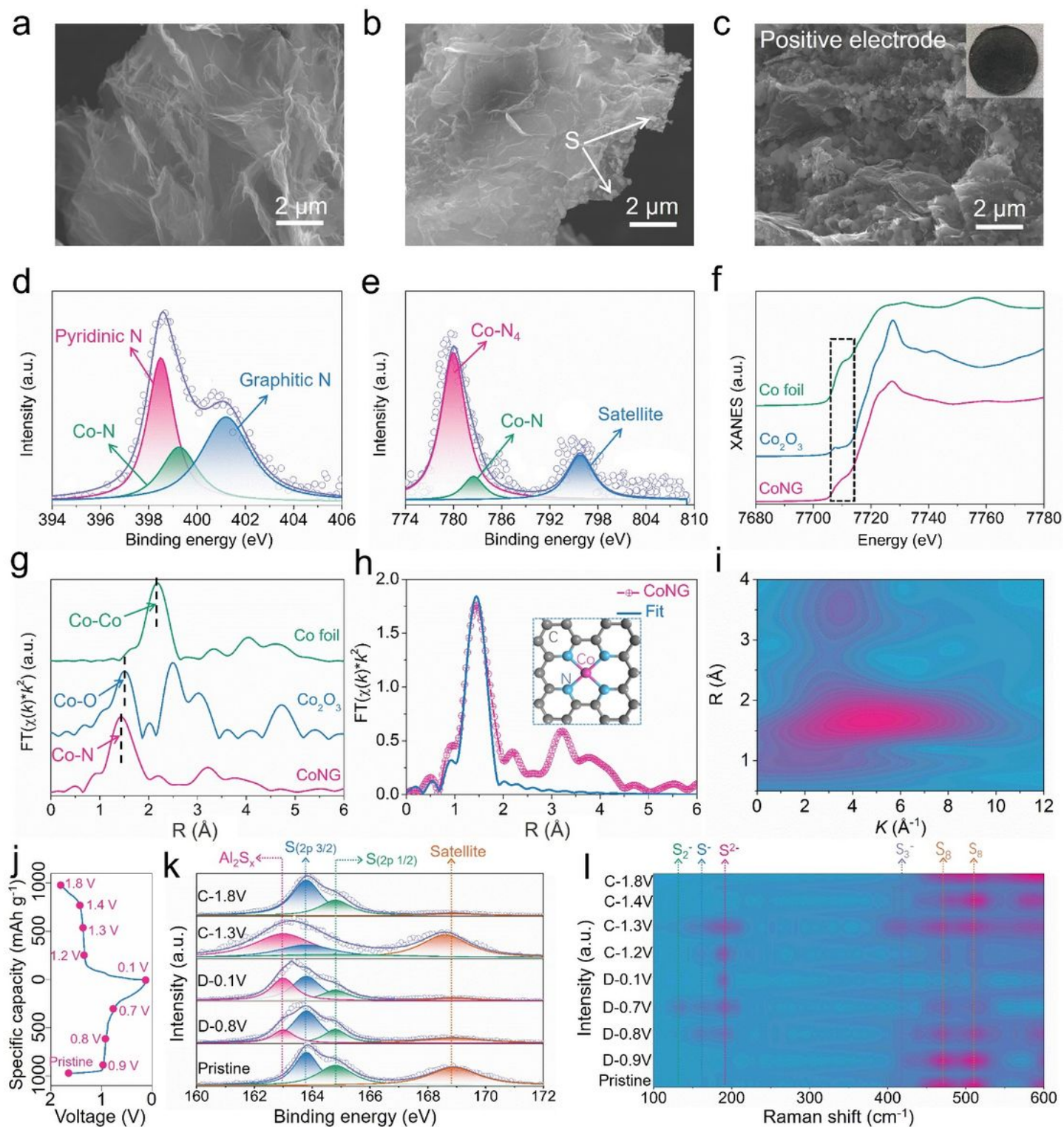


Figure 2

The structure characterization and evolution of sulfur positive electrode. (a) SEM morphology of CoNG. (b) SEM morphology of S@CoNG. (c) SEM morphology of composite positive electrode (the inset shows the photos of positive electrode pallets). The XPS spectra of N 1s (d) and Co 2p (e) for CoNG. (f) Co K-edge XANES spectra of CoNG, Co₂O₃, and Co foil. (g) Co K-edge FT-EXAFS in R space of CoNG, Co₂O₃, and Co foil. (h) Co K-edge EXAFS fitting of CoNG in R space (inset: the corresponding schematic model of

Co-N₄). **(i)** Wavelet transforms for CoNG. **(j)** The charge and discharge curves of S@CoNG-based Al-S battery (the pink dots indicate that the batteries are disassembled for subsequent characterization after being charged and discharged to different voltages). **(k)** The XPS spectra of S 2p for S@CoNG positive electrode with various charge/discharge state, the pristine sample, discharge to 0.8 V (D-0.8V) and 0.1 V (D-0.1V), and charge to 1.3 V (C-1.3V) and 1.8 V (C-1.8V). **(l)** The Raman spectra of S@CoNG positive electrode with various charge/discharge state, the pristine sample, discharge to 0.9 V (D-0.9V), 0.8 V (D-0.8V), 0.7 V (D-0.7V) and 0.1 V (D-0.1V), and charge to 1.2 V (C-1.2V), 1.3 V (C-1.3V), 1.4 V (C-1.4V) and 1.8 V (C-1.8V).

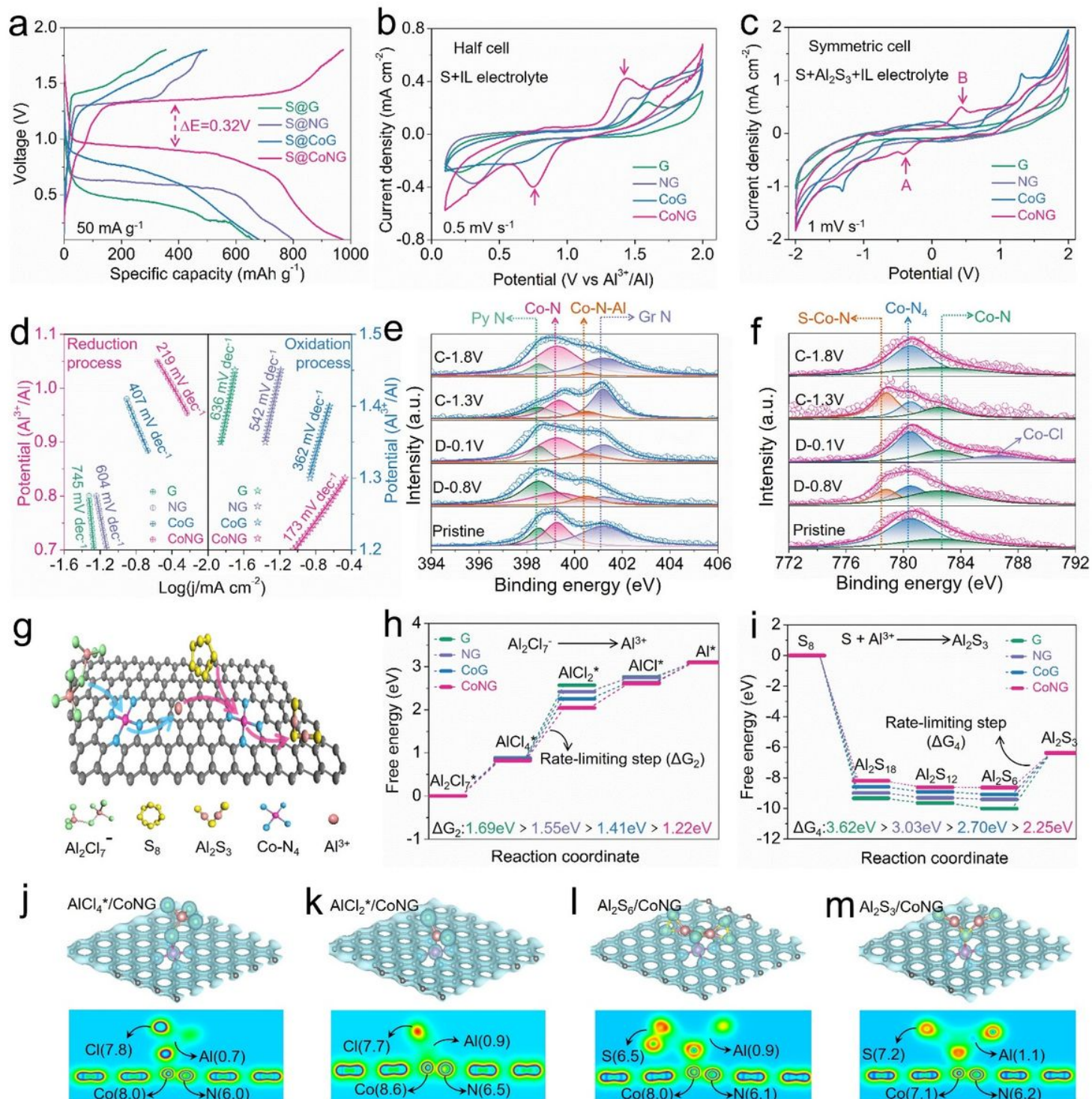


Figure 3

The electrocatalytic effect of CoNG on the sulfur conversion. (a) The charge and discharge curves of liquid-state Al-S batteries assembled with S@G, S@NG, S@CoG, and S@CoNG positive electrode. **(b)** The CV curves of half-cell assembled with G, NG, CoG, and CoNG working electrode and sulfur dissolved ionic liquid (S+IL) electrolyte. **(c)** The CV curves of symmetric cell assembled with G, NG, CoG, and CoNG electrode and sulfur and aluminum sulfide dissolved ionic liquid (S+Al₂S₃+IL) electrolyte. **(d)** Tafel plots for corresponding reduction and oxidation reactions of sulfur on G, NG, CoG, and CoNG. The XPS results of N 1s **(e)** and Co 2p **(f)** for S@CoNG positive electrode with various charge/discharge state. **(g)** Schematic illustration of the sulfur reduction on CoNG. **(h)** Energy profiles for the dissociation of chloroaluminate ions on G, NG, CoG, and CoNG substrates. **(i)** Energy profiles for the reduction of sulfur on G, NG, CoG, and CoNG substrates. The charge distribution of AlCl₄⁻ **(j)**, AlCl₂⁺ **(k)**, Al₂S₆ **(l)** and Al₂S₃ **(m)** on CoNG substrates.

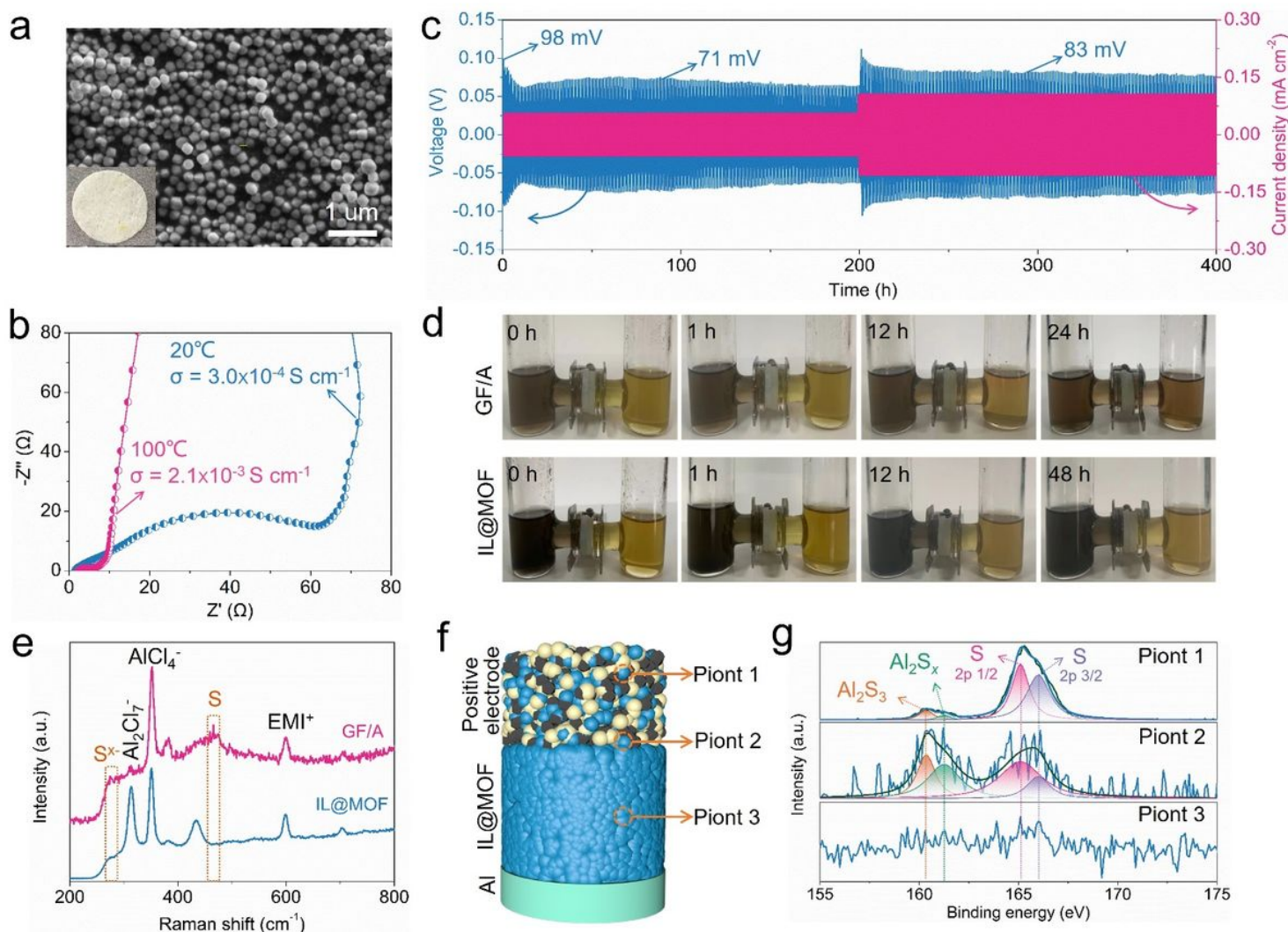


Figure 4

The electrochemical performance and restriction on polysulfide of IL@MOF quasi-solid-state electrolyte. **(a)** SEM morphology of IL@MOF particle (the inset shows the photos of IL@MOF pallet). **(b)** EIS plot of the Mo|IL@MOF|Mo symmetric cell at 20 °C and 100 °C. **(c)** Voltage profiles for the Al|IL@MOF|Al symmetric cell at current densities of 0.05 and 0.1 mA cm⁻². **(d)** Permeation tests for GF/A separators and IL@MOF electrolyte pallet. **(e)** Raman spectra of the solution in right chamber of H-type cell after permeation tests using GF/A separators and IL@MOF electrolyte pallet. Schematic diagram of the different points in the cycled quasi-solid-state Al-S battery **(f)** and the corresponding XPS spectra of S 2p **(g)**.

Supplementary Files

This is a list of supplementary files associated with this preprint. Click to download.

- [Supportinginformation.docx](#)
- [Onlinefloatimage5.png](#)